Can. J. Remote Sensing, Vol. 31, No. 1, pp. 73–84, 2005

A constant false alarm rate (CFAR) detector for RADARSAT-2 along-track interferometry

Shen Chiu

Abstract. Canada's RADARSAT-2 synthetic aperture radar (SAR) satellite will be equipped with an experimental ground moving target indication (GMTI) mode, which makes use of the "dual-receive" capability of the RADARSAT-2 antenna to provide two apertures aligned in the along-track direction. The mode allows two SAR images to be taken under identical geometry of observation, but separated by a short time lag. One of the GMTI techniques currently being explored is based on SAR along-track interferometry (SAR ATI), which uses the magnitude–phase information of the interferogram to extract movers from stationary clutter. In this paper, an unconventional but fully automatic detection scheme, derived using a histogram approximation to the clutter joint probability density function (PDF), is proposed. The new nonparametric method permits the implementation of a constant false alarm rate (CFAR) detector without deriving a theoretical joint PDF for the clutter interferogram. A false alarm reduction technique, based on "selective" local density calculations, is also discussed. Experiments show striking improvement in reducing the number of false alarms (up to 60% reduction) over the original detector without significantly degrading its performance. The detector is shown to be robust in its ability to handle both simulated (RADARSAT-2) and real (airborne) data. Comparison with a conventional parametric CFAR detector, derived using theoretical marginal PDFs of the magnitude and phase of the interferogram, suggests the performance superiority of the new detector.

Résumé. Le satellite radar canadien à synthèse d'ouverture (RSO) RADARSAT-2 sera équipé d'un mode expérimental GMTI (« ground moving target indication » – indication de cible mobile au sol) faisant usage de la capacité de réception à 2 fréquences de l'antenne de RADARSAT-2 à fournir deux ouvertures alignées dans la direction de la trace. Ce mode permet d'acquérir deux images RSO dans des conditions identiques de géométrie d'observation mais séparées par un court laps de temps. Une des techniques GMTI présentement sous analyse est basée sur l'interférométrie longitudinale RSO (ATI – « along-track interferometry ») et utilise l'information d'amplitude-phase de l'interférogramme pour extraire les objets mobiles du fouillis d'échos stationnaires. Dans cet article, on propose une procédure non conventionnelle mais entièrement automatique de détection basée sur l'utilisation de l'approximation par histogramme par rapport à la fonction de distribution de probabilité conjointe (FDP) du fouillis d'échos. La nouvelle méthode non paramétrique permet de mettre au point un détecteur de taux de fausse alarme constant (TFAC) sans qu'il ne soit nécessaire de dériver une FDP conjointe théorique pour l'interférogramme du fouillis. Une technique de réduction des fausses alarmes, basée sur des calculs de densité locale « sélective » est également discutée. Les expériences montrent des améliorations étonnantes dans la réduction du nombre de fausses alarmes (jusqu'à 60 % de réduction) par rapport au détecteur original sans qu'il n'y ait de dégradation de sa performance. Le détecteur s'est avéré robuste dans sa capacité à traiter des données simulées (RADARSAT-2) et réelles (aéroportées). Une comparaison avec un détecteur paramétrique conventionnel TFAC, dérivé en utilisant des FDP théoriques marginales de l'amplitude et de la phase des interférogrammes, tend à démontrer la performance supérieure du nouveau détecteur.
[Traduit par la Rédaction]

Introduction

Canada's RADARSAT-2 commercial synthetic aperture radar (SAR) satellite, scheduled to be launched in late 2005, will have an experimental mode that will allow ground moving target indication (GMTI) measurements to be made. This mode of operation is called MODEX for moving object detection experiment. The RADARSAT-2 MODEX is the world's first attempt to implement a limited-function GMTI onboard a commercial SAR satellite. Such a radar could be used to validate GMTI parameters and algorithms needed for more sophisticated radars. Preliminary information on the RADARSAT-2 MODEX configuration can be found in Luscombe (1995) and Livingstone (1998). **Table 1** lists some of the MODEX sensor characteristics and design parameters. In the MODEX mode, the spacecraft's radar antenna is partitioned into two apertures, aligned in the along-track direction, which record two echoes (the dual-receive mode), one from each wing, for every pulse transmitted at the full antenna. In addition to the dual-receive mode of operation, RADARSAT-2 will also support an alternating-transmit mode where pulses are transmitted alternately from each wing and received alternately on each wing. This mode allows greater separation of the two-way phase centres in the along-track direction. Data are coherently received from both apertures and are then downlinked in parallel channels for processing to extract moving target velocities in their SAR image context. The

Received 16 February 2004. Accepted 21 September 2004.

S. Chiu. Space-Based Radar Group, Radar Systems Section, Defence R&D Canada – Ottawa, 3701 Carling Avenue, Ottawa, ON K1A 0Z4, Canada (e-mail: shen.chiu@drdc-rddc.gc.ca).

Table 1. RADARSAT-2 MODEX parameters.

Orbit description	
Type	Circular
Inclination (°)	98.6
Altitude (km)	800
Active array	
Length (m) × width (m)	15 × 1.5
No. of subapertures	2
Orientation	Long axis forward; elevation boresight ± 29.5° (selectable)
Look geometry	
Nominal incidence angle (°)	10–60
Search type	Strip map
Swath size (km)	25–150
Azimuth beam width (°)	Programmable from 0.21 to 0.63
Detection cell size (m)	Programmable from 25 × 25 to 3 × 3
Waveform	
Band (GHz)	5.405
Bandwidth (MHz)	10–50
Peak radiated power (kW)	2.4 (42 μs pulse); 3.7 (21 μs pulse)
Duty ratio (%)	10
PRF (Hz)	1300–3800
Receiver noise temperature (K)	795.11

ground processing infrastructure for MODEX is presently being developed based on the theoretical understanding of the measurement process, augmented and validated by airborne SAR GMTI experiments (Livingstone et al., 2002) and simulation studies (Chiu, 2000a; 2000b) that emulate the RADARSAT-2 radar performance and observation geometries.

One of the proposed RADARSAT-2 GMTI processor architectures uses SAR along-track interferometry (SAR ATI) signal magnitude and phase information to extract slow ground movers from stationary background clutter. The application of the SAR interferometry technique to GMTI has been examined by other investigators (Soumekh, 1997; Ender, 1999; Moccia and Rufino, 2001). The SAR ATI processor uses two displaced phase centres aligned along track, and an interferogram is formed by taking the product of one image with the complex conjugate of the other after the two image datasets have been coregistered in time via a delay operator. When viewed in the complex plane as a two-dimensional (2D) magnitude (radius) and phase (angle) distribution, the complex signal output of the SAR ATI processor results in a bell-shaped distribution as seen in **Figure 1**. Here, stationary scatterers in the imaged terrain are represented by their phase-noise distribution about the zero-phase axis. Moving targets appear at nonzero phase angles that are proportional to the slant-range velocities of the targets. It is clear from **Figure 1** that moving target detection via the SAR ATI approach is a 2D process. The conventional approach to constant false alarm rate (CFAR) detection would, therefore, require elaborate statistical modeling of the stationary clutter interferogram. This paper reports on an adaptive nonparametric CFAR detection scheme that is simple to implement and does not involve theoretical modeling of clutter statistics.

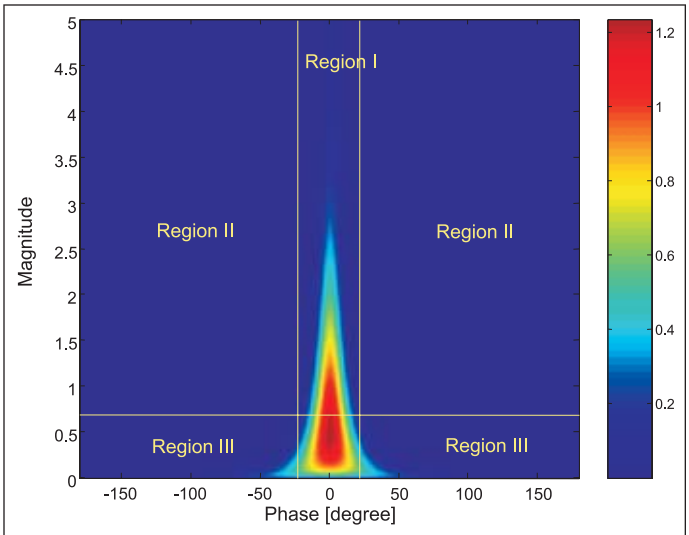

Figure 1. Theoretical joint probability density function of the one-look ($n = 1$) along-track interferometric phase ψ and magnitude ξ. The coherence between the two one-look images is $\rho = 0.981$.

The paper shows the shortcomings of conventional CFAR detection schemes and gives the rationale for advocating a nonparametric CFAR approach and for using a threshold function $\gamma(\psi)$. The proposed adaptive nonparametric CFAR detector is then described in detail. The new detector is tested using both simulated spaceborne data and experimental airborne data, and the results are described and discussed, followed by a summary of the findings.

Clutter models

Homogeneous (Gaussian) clutter

The quadrature components of received echoes from the stationary clutter are often modeled as zero-mean Gaussian processes, implying Rayleigh distributed magnitude. The model is warranted for rough (on the scale of the radar wavelength) but homogeneous backscatterers because the sum of independent, identically distributed (i.i.d.) scatterers is complex Gaussian distributed by the central limit theorem. This assumption has been validated over homogeneous agricultural and natural areas such as forest and open field areas but breaks down over more heterogeneous or smooth surfaces such as urban areas or sea surfaces (Conte et al., 1991). The detailed derivation of probability density functions (PDFs) of the complex interferogram under the assumption of jointly Gaussian distributed data has been described by Lee et al. (1994a; 1994b) and Joughin and Winebrenner (1994). The results are summarized here.

For a two-channel SAR system, such as RADARSAT-2, one defines the column vector $\boldsymbol{x} = [x_1\ x_2]^{\mathrm{T}}$ with elements $x_i = P_i^{1/2} z_i$, where z_i is a complex normally distributed variable, P_i is the mean power level of the ith channel, and T is the transpose operator. The vector $\boldsymbol{x}$ is modeled as a bivariate complex Gaussian random vector with PDF

$$f_{\boldsymbol{x}}(\boldsymbol{x}) = \frac{1}{\pi^2 \det(\mathbf{R})} \exp(-\boldsymbol{x}^{\mathrm{H}}\mathbf{R}^{-1}\boldsymbol{x}), \tag{1}$$

where $\mathbf{R}$ is the clutter (plus noise) covariance matrix, the superscript H is the complex conjugate transpose operator, and $\det(\mathbf{R})$ is the determinant of $\mathbf{R}$. The covariance matrix $\mathbf{R}$ can be written as

$$\mathbf{R} = E\{\boldsymbol{x}\boldsymbol{x}^{\mathrm{H}}\} = \begin{bmatrix} P_{\mathrm{c},1} & \sqrt{P_{\mathrm{c},1}P_{\mathrm{c},2}}\exp(j\theta) \\ \sqrt{P_{\mathrm{c},1}P_{\mathrm{c},2}}\exp(-j\theta) & P_{\mathrm{c},2} \end{bmatrix}$$

$$+ P_{\mathrm{n}}\mathbf{I} = \begin{bmatrix} P_1 & \sqrt{P_1P_2}\rho\exp(j\theta) \\ \sqrt{P_1P_2}\rho\exp(-j\theta) & P_2 \end{bmatrix}, \tag{2}$$

where $E\{\cdot\}$ denotes the expectation value of the parameters in parentheses, $P_i = P_{\mathrm{c},i} + P_{\mathrm{n}}$ (where $P_{\mathrm{c},i}$ is the clutter power from the ith channel, and P_{n} is the noise power), $\mathbf{I}$ is the 2×2 identity matrix, $\rho\exp(j\theta)$ is the complex correlation coefficient between the two channel outputs, and

$$\rho = \sqrt{\frac{P_{\mathrm{c},1}P_{\mathrm{c},2}}{P_1P_2}} \tag{3}$$

The off-diagonal elements $R_{12} = R_{21}^{*} = (P_1P_2)^{1/2}\rho\exp(j\theta)$ describe the complex interferogram. While the phase θ of the across-track interferogram depends on the illumination geometry and terrain elevation, the phase of the along-track interferogram is assumed zero for stationary clutter ($\theta = 0$). In the case of internal clutter motion, such as sea surface currents, θ is a function of the current velocity.

To reduce speckle, the data are multilook processed, which requires averaging several independent one-look interferograms. Whether multilooking is advisable for the SAR ATI (reduction of target peak amplitude versus reduction of phase noise) has been discussed by Gierull and Sikaneta (2002). The sample covariance matrix is given as

$$\overline{\mathbf{R}} = \frac{1}{n}\sum_{k=1}^{n}\boldsymbol{x}_k\boldsymbol{x}_k^{\mathrm{H}} = \frac{1}{n}\mathbf{Q} = \frac{1}{n}\begin{bmatrix} Q_{11} & \alpha\exp(\mathrm{j}\psi) \\ \alpha\exp(-j\psi) & Q_{22} \end{bmatrix} \tag{4}$$

where n is the number of looks, $\boldsymbol{x}_k$ is the kth look sample, and the phase difference ψ (or the interferometric phase) is the argument of the upper off-diagonal term in the matrix $\mathbf{Q}$. The samples are assumed to be statistically independent, but in reality certain dependence between samples occurs. In such a case, the statistical dependence can be accounted for by using an effective number of looks (Joughin and Winebrenner, 1994; Gierull and Sikaneta, 2002). The random matrix $\mathbf{Q}$ is well known to be complex Wishart distributed (Goodman, 1963), with a probability density function as follows:

$$f_{\mathbf{Q}}(\mathbf{Q}) = \frac{\det(\mathbf{Q})^{n-2}}{\pi\Gamma(n)\Gamma(n-1)\det(\mathbf{R})^{n}}\exp[-\mathrm{tr}(\mathbf{R}^{-1}\mathbf{Q})]$$

$$\text{for } n = 2, 3, 4\ldots, \tag{5}$$

where $\mathrm{tr}(\cdot)$, $\det(\cdot)$, and $\Gamma(\cdot)$ denote the trace, the determinant, and the gamma function of the parameters in parentheses. The matrix $\mathbf{Q}$ is positive definite. By setting $\Delta_1 = Q_{11}/P_1$, $\Delta_2 = Q_{22}/P_2$, and $\eta = \alpha(P_1P_2)^{-1/2}$, Equation (5) can be simplified to

$$f(\Delta_1, \Delta_2, \eta, \psi) = \frac{(\Delta_1\Delta_2 - \eta^2)^{n-2}\eta}{\pi(1-\rho^2)^{n}\Gamma(n)\Gamma(n-1)}$$

$$\times\exp\left[-\frac{\Delta_1 + \Delta_2 - 2\eta\rho\cos(\psi-\theta)}{1-\rho^2}\right] \tag{6}$$

where η is the magnitude and ψ the multilook phase of the interferogram. By a change of variable $\xi = \eta/n$ (the normalized multilook magnitude) and by integrating with respect to Δ_1 and Δ_2 from 0 to ∞, the PDF in Equation (6) becomes

$$f(\xi, \psi) = \frac{2\eta^{n+1}\xi^{n}\exp\{[2n\xi\,\rho\cos(\psi-\theta)]/(1-\rho^2)\}}{\pi\Gamma(n)(1-\rho^2)}$$

$$\times K_{n-1}\left(\frac{2n\xi}{1-\rho^2}\right), \qquad \text{for } n = 1, 2, 3, \ldots, \tag{7}$$

where $K_{n-1}(\cdot)$ is a modified Bessel function of the second kind. Note that even though Equation (5) is not defined for $n = 1$, Equation (7) is defined.

An example of the PDF $f(\xi,\psi)$, computed from Equation (7) for $n = 1$ and $\rho = 0.981$, is plotted in **Figure 1**, which shows the typical behavior of the phase fluctuation (variance): large fluctuation for small clutter magnitudes and small fluctuation for large radar returns. For an ideal, "noise-free" radar and rigorously stationary scatterers, stationary interferometric scene elements would be completely coherent and would map to the zero-phase axis. Partial decorrelation of the radar signals over the SAR aperture time results in the measured points being clustered in the vicinity of the zero-phase axis. Decorrelation mechanisms include additive thermal noise and multiplicative phase noise of the radar (Chiu and Livingstone, 2005), and "internal" motion of clutter over the observation period. In the magnitude–phase plane, the additive noise will appear as a point distribution about the zero-phase axis, and the root mean square (RMS) width of the distribution is independent of the signal strength. The phase noise also appears as a distribution about the zero-phase axis, but whose RMS width limits to a constant phase angle for large-amplitude signals. Increasing the number of independent looks leads to speckle reduction and hence smaller variance, even for moderate interferogram magnitudes.

Integrating Equation (7) over the normalized magnitude ξ from 0 to ∞ leads to the marginal multilook density function for the phase ψ:

$$f_\psi(\psi) = \frac{\Gamma(n+1/2)(1-\rho^2)^n \rho\cos(\psi-\theta)}{2\sqrt{\pi}\Gamma(n)[1-\rho^2\cos^2(\psi-\theta)]^{n+1/2}} + \frac{(1-\rho^2)^n}{2\pi}$$

$$\times F[n,1;1/2;\rho^2\cos^2(\psi-\theta)] \qquad \text{for } -\pi < \psi \le \pi, \qquad (8)$$

where $F(\cdot)$ is the Gauss hypergeometric function given by

$$F(a,b;c;z) = \frac{\Gamma(c)}{\Gamma(a)\Gamma(b)} \sum_{k=0}^{\infty} \frac{\Gamma(a+k)\Gamma(b+k)}{\Gamma(c+k)} \frac{z^k}{k!} \qquad \text{for } |z|<1$$

The marginal PDF in Equation (8) depends only on the number of looks and the magnitude of the complex correlation coefficient ρ. The peak of the distribution is located at $\psi = \theta$. In along-track interferometry, ψ should be centred around zero for stationary clutter. Multilook processing reduces the statistical phase fluctuation, i.e., the variance of the phase decreases for a large number of looks. The width of the distribution depends on the correlation coefficient ρ. The PDF reduces to a uniform distribution for $\rho = 0$ and a Dirac delta function (or distribution) for $\rho = 1$.

Similarly, integrating Equation (7) with respect to the phase ψ (from $-\pi$ to π) leads to the marginal multilook density function for the multilook magnitude ξ:

$$f_\xi(\xi) = \frac{4n^{n+1}\xi^n}{\Gamma(n)(1-\rho^2)} I_0\left(\frac{2n\xi\rho}{1-\rho^2}\right) K_{n-1}\left(\frac{2n\xi}{1-\rho^2}\right), \qquad (9)$$

where $I_0(\cdot)$ is the modified Bessel function of zero order of the first kind.

Heterogeneous (non-Gaussian) clutter

The implementation of a CFAR detector suitable for the SAR ATI involves a 2D detection process, which requires elaborate statistical modeling of the magnitude and phase of the terrain interferogram, and the derivation of their joint PDF. Analytical studies of the statistics of the phase and magnitude of the interferogram are very rare for non-Gaussian SAR image distributions, and the joint magnitude–phase PDF for general, non-Gaussian image distributions cannot be modeled analytically.

It was shown that the theoretical marginal PDF of the phase of the interferogram in Equation (8), derived under the assumption of Gaussian backscatters, agrees almost perfectly with real data for a wide variety of backscatter conditions (Gierull, 2001). **Figure 2** shows two representative results illustrating the observed phase distribution invariability. The set of data used in **Figure 2** was taken from an airborne GMTI experiment conducted in July 1999 at Canadian Forces Base (CFB) Petawawa; the same dataset is the basis for the experiments in this study to test the performance of the proposed new CFAR detection scheme. The clutter type within patch 1 corresponds to low-scrub vegetation, and patch 24 is thickly covered with jack pine; see Gierull (2001) for the image patches from which the histograms have been computed. These results agree well with other, mainly polarimetric studies that have reported similar findings (Lee et al., 1994a; 1994b; Joughin and Winebrenner, 1994).

The corresponding marginal PDF for magnitude, on the other hand, deviates strongly from the measured data in most cases, even in homogeneous scenes, as shown in **Figure 2**. This is especially true in highly heterogeneous composite terrains such as over urban areas. In such cases, the observed distributions show longer tails and larger variance-to-expectation ratios (spiky clutter) than those predicted by Gaussian distribution. It becomes clear that a simple magnitude PDF cannot accommodate all the different scenarios. One might instead consider a class or family of distributions, in which Rayleigh distribution must be a member. Among such distributions, the Weibull and the *K* distributions have received a great deal of attention in the literature (e.g., Conte et al., 1991; Frery et al., 1997). These distributions result from a compound or, often called, multiplicative model for the clutter and have been shown to fit a wide range of experimental data well. However, even the *K* distribution sometimes fails to model extremely heterogeneous terrains such as urban areas, i.e., scenes that contain different landscape types. Gierull (2001) has derived a new density function, called the *p* distribution, for the magnitude of the interferogram for heterogeneous terrain based on a recently proposed generalized distribution for the texture statistic of the SAR image magnitude (Frery et al., 1997). The *p* distribution was shown to match real data more accurately, but its use requires sometimes-unstable numerical methods. The problem of numerical stability in the practical implementation of a CFAR detector needs to be addressed further. Moreover, highly heterogeneous terrains are still not satisfactorily modeled by the *p* distribution.

In addition to overcoming the challenge of modeling the magnitude PDF of the terrain interferogram, one has yet to address the proper modeling of the joint phase–magnitude PDF, instead of treating the marginal phase and magnitude PDFs separately. Gierull (2001) has proposed a CFAR detector based on estimating the magnitude and phase thresholds separately from theoretical marginal PDFs for magnitude and phase, rather than deriving a threshold function $\gamma(\psi)$ from the joint magnitude–phase PDF. The distribution of the interferometric magnitude is clearly a function of the interferometric phase, however, and treating only the marginal distributions leads to the problem of detecting only moving targets falling in region II of the ξ–ψ plane in **Figure 1**, but regions I and III are completely missed by this detection scheme. The detection method based on marginal PDFs does not optimize the probability of detection (P_D) because it is basically a two-step filtering process and does not take into account explicitly the phase dependence of the magnitude threshold $\gamma(\psi)$. Therefore, the detector is expected, in principle, to perform more poorly than a detector that utilizes a joint ξ–ψ PDF for its detection

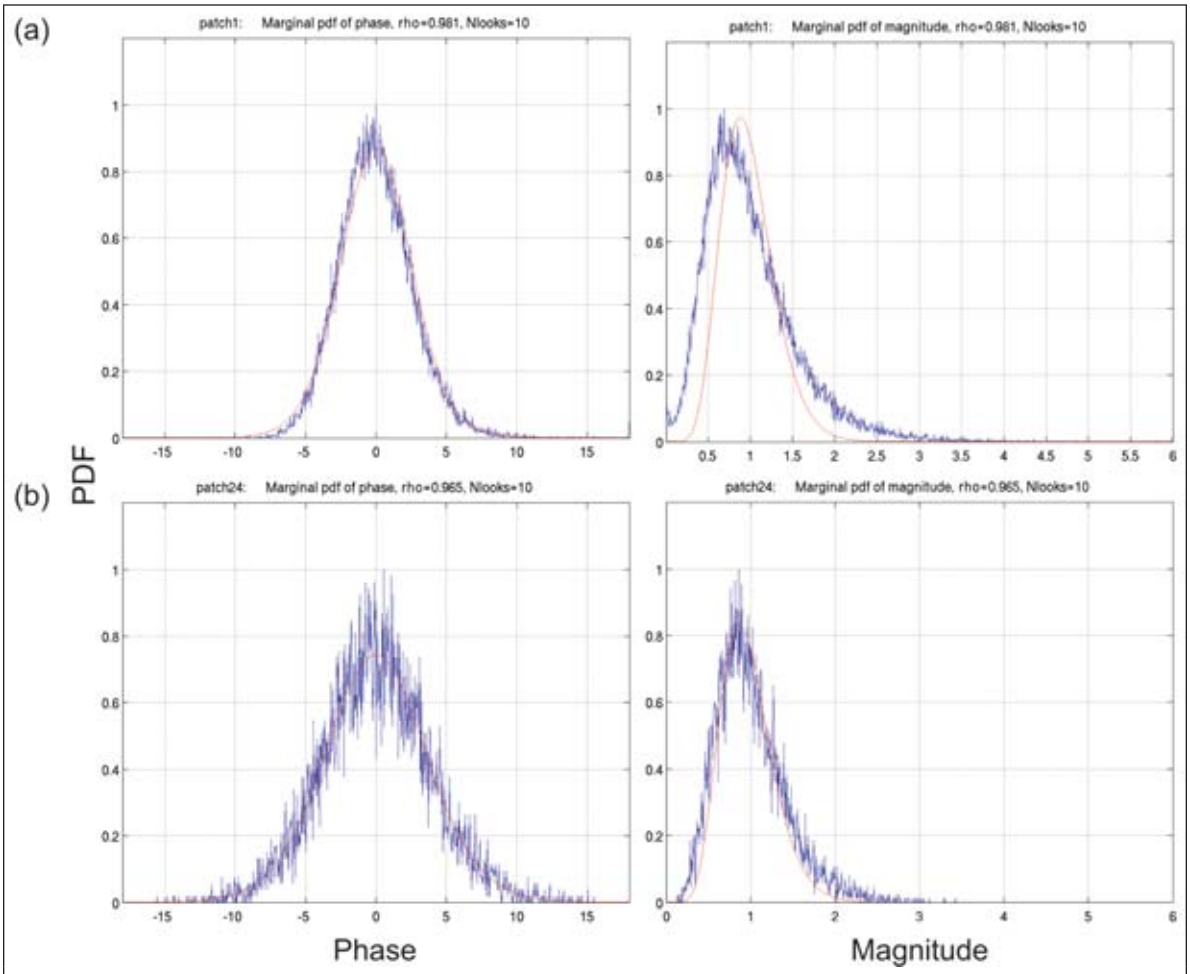

Figure 2. Comparison of the theoretical density functions and empirical histograms of the magnitudes and phases for SAR ATI measurements on two homogeneous areas with different terrain cover: (a) patch 1, $\rho = 0.981$, number of looks = 10; (b) patch 24, $\rho = 0.965$, number of looks = 10. The smooth lines are theoretical PDFs.

scheme. In this respect, an alternate approach to CFAR detection, specifically one that does not require the theoretical derivations of the interferogram's magnitude and phase PDFs but takes into account the phase dependence of the magnitude threshold $\gamma(\psi)$, is desirable and of great practical value.

A nonparametric approach to CFAR detection

In the parametric approach to CFAR detection, background noise or clutter distributions are assumed known except for a finite number of parameters, and the distribution type is fixed except for possible variation in one or more distribution parameters. Nonparametric detectors, on the other hand, provide detection with no a priori assumptions on the form of the background noise or clutter distributions.

This paper reports on the implementation of a nonparametric CFAR detection scheme that is suitable for the SAR interferometry. The technique estimates the magnitude–phase joint PDF of the terrain interferogram via a histogram-binning procedure and computes an approximate probability of false alarm P_{FA} without deriving the theoretical joint PDF for the stationary clutter.

The magnitude threshold $\gamma(\psi)$, which maximizes the probability of detection P_D, is a function of the interferometric phase ψ and is dependent on target PDFs and radar cross sections (RCSs). Since the target parameters (or characteristics) may not be known, the optimization of P_D is not at all trivial. If one were to use a constant-magnitude threshold, $\gamma(\psi) = \xi_c$ (where ξ_c is a constant-magnitude value), for all phase angles or a constant-phase threshold, $|\psi| = \psi_c$ (where ψ_c is constant-magnitude value), for all magnitude values, then the result would lead to either too many false alarms or too few detected targets. One possible choice of $\gamma(\psi)$, which takes into account the phase dependence of the magnitude PDF, is to use constant-density contour lines from the joint PDF $f(\xi, \psi)$, if it can be theoretically derived. This has proven to be very challenging, however, and the derived PDF often fails for highly heterogeneous terrains.

Here we take an approach that does not require the derivation of a theoretical joint PDF for the terrain interferogram but takes into account the dependence of a magnitude threshold γ on the

phase ψ. We first form a 2D histogram of the magnitude and phase of the interferogram by a simple histogram-binning procedure. The goal of this exercise is to obtain the constant-density contour lines of the bell-shaped distribution (**Figure 1**). These lines represent the histogram approximation of the theoretical magnitude–phase threshold functions γ(ψ), from which one can separate the movers from the clutter and calculate P_{FA}. The P_{FA} is specified with one of these contour lines chosen as the approximate magnitude threshold function γ(ψ). One may also fix the number of signal dots in a magnitude–phase bin (say two dots per bin) and vary the bin size (or the number of bins) to specify an equivalent set of density contour lines. The former approach of histogram binning (based on a fixed bin size and a varying number of dots per bin) gives coarser P_{FA} increments and is not very suitable for constructing a CFAR detector that can be fine-tuned to a wide range of P_{FA} values. In the following analysis, however, the former (or the first) approach is chosen to explain the key ideas, on which the proposed detector is based, because it can be more easily understood conceptually.

If the joint PDF $f(\xi, \psi)$ of the stationary clutter is known, then in principle one can find the constant-density contour lines in the ξ–ψ plane for which $f(\xi, \psi) = C$, where C is a constant. The contour lines are denoted as $\gamma(\psi, C)$. The constant C can be determined for a fixed P_{FA} via Equation (10) as

$$P_{FA} = \int_{-\pi}^{\pi} \int_{\gamma(\psi)}^{\infty} f(\xi, \psi)\, d\xi\, d\psi \tag{10}$$

where ξ is the magnitude of the interferogram, ψ is the phase of the interferogram, and γ(ψ) is the threshold function of the joint PDF $f(\xi, \psi)$. Once C has been determined as a function of P_{FA}, the contour lines depend implicitly on P_{FA}. The proposed histogram-binning approach essentially approximates Equation (10) by computing the approximate P_{FA} from

$$P_{FA} \approx \frac{\sum_{x_i \in R} \text{count}(x_i)}{N_{tot}}, \tag{11}$$

where $\text{count}(x_i)$ is the number of dots in bin x_i, R is the set of all bins with a count below or equal to a threshold but greater than zero, and N_{tot} is the total number of sample points. The expression in Equation (11) sums all the signal dots in the magnitude–phase bins with the number of dots in the range $0 <$ count $\le$ threshold and divides it by the total number of signal dots to yield P_{FA}. Equation (11) gives correct P_{FA} values if there are no moving targets. When the movers are present, the approximation remains good if there are significantly more false alarms than targets, otherwise it remains poor. To take into account the presence of the moving targets, one modifies the R set of all bins with a count below a threshold to a new set of all bins belonging to the region between the chosen constant-density threshold contour line, or the approximate threshold function γ(ψ), and the outermost contour line defined in the next paragraph. The proposed detection scheme makes use of the following observations or facts about the joint PDF of the stationary clutter: (*i*) the magnitude ξ distribution is a function of interferometric phase ψ; (*ii*) the tail of the ξ distribution becomes longer as ψ approaches zero, and the signal samples are more dispersed in the ξ–ψ plane at large ξ values; (*iii*) away from ψ = 0, the ξ distributions have increasingly shorter tails, and signal samples are closely clustered together; and (*iv*) for well-balanced channels, the clutter joint PDF is symmetric and has a bell-shaped distribution in the ξ–ψ plane.

The previous observations are true even for non-Gaussian heterogeneous terrains. These observations allow us to say that signal points outside the symmetric bell-shaped distribution are most likely those of moving targets. The fact that stationary terrain signal samples are closely clustered together away from zero phase position ($|\psi| > 0$) and the fact that movers outside the bell-shaped distribution are well dispersed allow one to define the outermost contour line to be the one that has the lowest density while retaining the bell-shaped symmetry. A contour line obtained from a histogram is never perfectly symmetric, however. One can use the Marola Symmetry Metric (Marola, 1989) to measure the symmetry of the line and decide when the symmetry is broken. The implicit assumption of the detection scheme is that the movers are rare events in a dominant background of the stationary clutter. Therefore, the sample size (i.e., the total number of samples) needs to be large enough to ensure that there are significantly more clutter points than those of movers in order for the proposed scheme to work. Typically, 10^5 samples are used in this study. The region near zero phase (ψ = 0) needs special attention, since the magnitude (ξ) distribution tends to be long-tailed and the signal samples are dispersed at large ξ values, making them indistinguishable from the movers if only the density criterion is used to differentiate them from the moving targets. For the proposed detector, one simply notches out this region and considers it to be all clutter. The width of the phase notch filter can be estimated from the phase noise of the system, whose RMS width is limited to a constant phase angle for large-amplitude signals. Equation (11) can therefore be redefined as

$$P_{FA} \approx \frac{\sum_{x_i \in \Re} \text{count}(x_i)}{\aleph_{tot}} \tag{12}$$

where $\Re$ is the set of all bins in the region outside the notched-out zero phase region and between the threshold function γ(ψ) and the outermost contour line; and $\aleph_{tot}$ is the total number of samples in the region bounded by the outermost contour line, including also the notched-out region (as illustrated in **Figure 3**). The desired P_{FA} is obtained from the proper choice of a threshold function or contour line. In the following sections, the new detector performance is tested against two sets of interferogram data obtained from RADARSAT-2 simulation and airborne experiments.

Experimental definition

Simulation

The simulated RADARSAT-2 MODEX data were obtained using a space-based MTI radar simulator known as SBRMTISIM (Nohara et al., 1999), developed by Sicom Systems Ltd. for the Canadian Department of National Defence (DND). The simulator provides an interactive environment definition module, which allows the user to specify the look geometry and define clutter regions and targets to create a scenario. Clutter is modeled as a dense set of regularly spaced scatterers with user-specified cross sections, scattering statistics, and internal motion. Targets are modeled as point scatterers with user-specified velocities, cross sections, and fading statistics. Other modules are provided to specify the radar and antenna parameters along with other parameters needed to characterize the system. Once these parameters are specified, the simulator generates high-fidelity, complex base-band signals representing the signals received by the radar. For more details of the simulator see Nohara et al. (1999) and Chiu (2000a; 2000b).

The simulation was carried out using a 12 MHz bandwidth chirp waveform, which yields ground range resolution of 25 m at a 30° incidence angle. The azimuth resolution was kept constant at 25 m. Simulations were performed on a targets-plus-clutter scene over a 1.5 km range swath, which contained a 2.5 km × 5.0 km land clutter patch with a reflectivity of –10 dB m^2/m^2 and a spectral width of 0.1 m/s (to model internal motions of vegetation). The clutter amplitude was Rayleigh distributed, the clutter phase was uniformly distributed, and the land patch was statistically stationary. Twenty targets, moving either eastward or westward, were generated within the simulated land surface. The velocities of the targets range from 15 to 64 km/h, and RCS is kept at 45 m^2. The satellite heading is approximately north (i.e., 98.6° inclination), with a right-looking geometry.

Airborne experiment

As part of the preparatory work for the RADARSAT-2 MODEX, airborne experiments were conducted to acquire SAR ATI data for typical RADARSAT-2 resolution and incidence angles. A dataset was obtained at CFB Petawawa on 14 July 1999 by the Environment Canada CV 580 C-band SAR configured in its along-track interferometer mode. The details of the experiment can be found in Livingstone et al. (2002) and are only briefly described here.

The CFB Petawawa training area was used as the primary experiment site (**Figure 4**). It had three direct-fire moving target ranges (called Delta, Juliet, and MIT) situated on flat, open spaces of sparse, herbaceous and shrubby vegetation in well-drained soil. Five controlled ground moving targets of differing types were used in the experiment. The Delta, Juliet, and MIT transport systems consisted of rail tracks and rail vehicles programmable to move at predetermined speeds. Two of the dirt roads (Steward Road and Messer Road) on the site provided paths for global positioning system (GPS) monitored truck targets (two pickup trucks). Each controlled moving target was equipped with a trihedral corner reflector and a

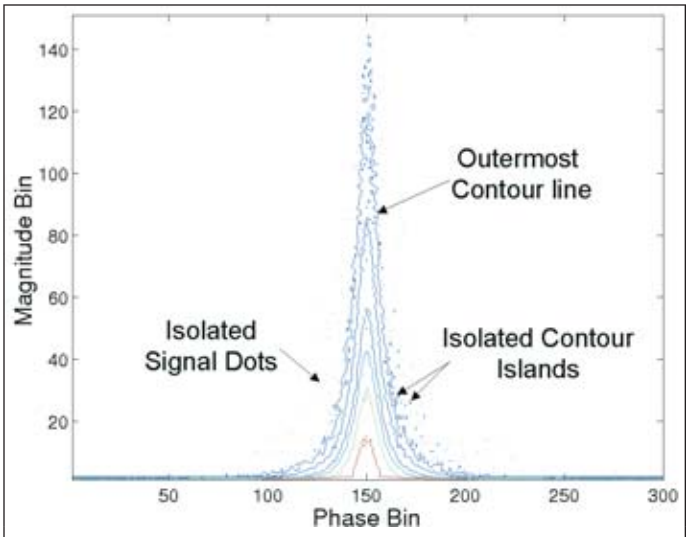

Figure 3. Two-dimensional histogram contour plot of magnitude–phase distribution of the SAR ATI signal.

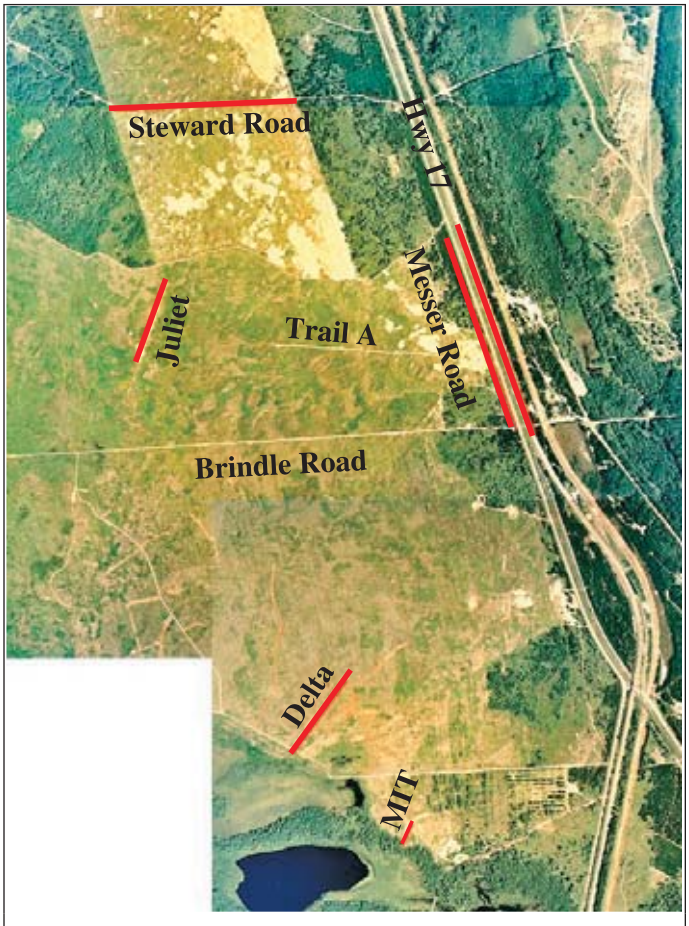

Figure 4. Aerial photograph mosaic of the CFB Petawawa training area. The Juliet (700 m) and Delta (650 m) target transport systems are labeled.

Table 2. Controlled ground moving targets.

Mover ID	Carrier	Track bearing angle (°)[a]	Speed (km/h)	Corner reflector RCS (m^2)
Juliet range	Carrier on a level rail	0	20 (P7, P8); 30 (P9, P10)	706
Delta range	Carrier on a level rail	18	10 (P7, P8); 20 (P9, P10)	309
MIT range	Carrier on a level rail	355	5 (all passes)	24
Stewart Road	Truck on gravel road	69	50 (P7, P8); 70 (P9, P10)	434
Messer Road	Truck on dirt road	323	40 (P7, P8); 60 (P9, P10)	432

[a]Measured clockwise from true north.

carrier-phase GPS receiver. Target velocities were selected to provide radial velocities between 5 and 70 km/h, both within the directional ambiguity speed. The details of the controlled targets are shown in **Table 2**.

Results and discussion

Simulation

The simulated RADARSAT-2 data are SAR processed, and an interferogram is formed via the SAR ATI processing chain. Plotting the resulting interferogram in magnitude versus phase format, one obtains a bell-shaped distribution for the stationary terrain interferogram, shown as dots in **Figure 5**. The dots with squares around them are moving target interferogram samples. The signals of the moving targets protrude from the bell-shaped clutter distribution. The goal of a CFAR detector is to automatically differentiate the targets from the clutter background, that is, the dots with squares from the simple dots, and to maintain a constant probability of false alarms for a varying clutter background. One cannot distinguish those dots with squares (moving target signals) falling inside the bell-shaped distribution from stationary terrain signal dots, because there is no magnitude–phase information about these targets that sets them apart from the terrain background. The proposed detection procedure considers those dots with squares falling outside the bell-shaped distribution to be the moving targets and everything else to be stationary clutter.

Figure 3 shows the contour plot of the distribution in **Figure 5**. The outermost contour line of the stationary clutter retains its bell-shaped symmetry. The moving targets, on the other hand, do not generally have symmetric PDFs about $\psi = 0$ because of their radial velocity components; and being rare events in the whole sample space, they appear either as isolated signal dots or as small isolated contour "islands" in a contour plot (see **Figure 3**). By choosing different threshold functions or threshold contour lines, one can calculate the P_{FA} from Equations (11) and (12), and the results are shown in **Figure 6**. The true P_{FA} values are also shown for comparison. The P_{FA} value calculated based on Equation (11) improves in accuracy as the number of false alarms increases, but it is poor at low P_{FA}. This is understandable because at low P_{FA} the contribution from the movers becomes non-negligible with respect to the total number of false alarms. The P_{FA} computed from the modified $\Re$ set improves the approximation dramatically and keeps the errors to within 30%, and the results are much less sensitive to the ratio of target to false alarm.

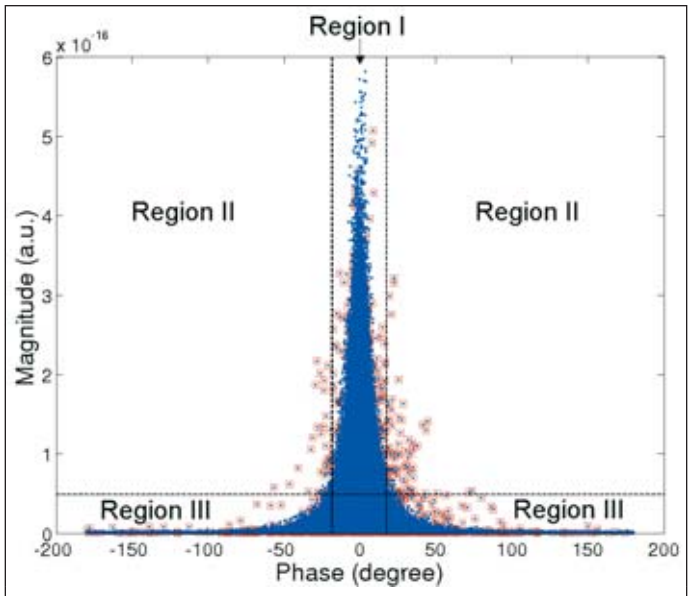

Figure 5. Magnitude versus phase of the SAR ATI signal.

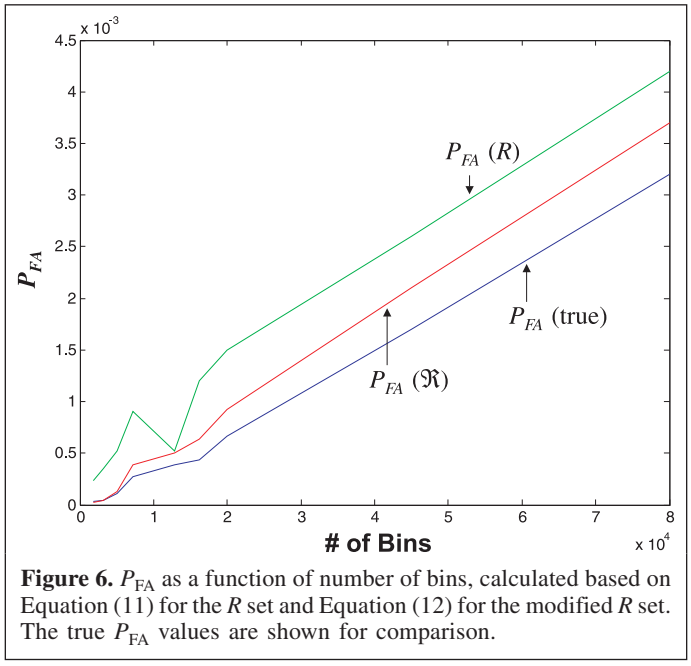

Figure 6. P_{FA} as a function of number of bins, calculated based on Equation (11) for the R set and Equation (12) for the modified R set. The true P_{FA} values are shown for comparison.

The moving targets are extracted by treating the set of all bins with a count lower than or equal to the threshold function as the movers plus false alarms; the detector outputs the result as shown in **Figure 7**. The method is surprisingly simple but effective, and it is automatic. For a P_{FA} of 3.0×10^{-5} (10 false alarms in a 2170×152 element scene), it detects 19 out of 20 targets. Note the targets have range migrated over the synthetic aperture time, and therefore they appear over several range bins as seen in **Figure 7**. Multiple detections of the same target are counted only once in the counting process.

The detection performance of the proposed detector is expected to be better than that of the marginal PDF-based CFAR detection scheme proposed by Gierull (2001). Preliminary results of the comparison of the two approaches showed that the current method is superior in performance when the two detection schemes were applied to the same sets of simulated data, particularly for slowly moving targets. When applied to the current set of data (i.e., **Figure 5**), for example, Gierull's approach detected 12 out of 20 targets for the same number of false alarms (see **Figure 8**).

Upon closer examination of the histogram-based detector, one realizes that there are always "edge" clutter points along the bell-shaped distribution that are "counted" as moving targets owing to the nature of histogram binning (see **Figure 9**). The magnitude–phase histogram binning approximates the true PDF but does not always reflect its true local densities at the edge of the bell-shaped distribution. Some of the edge bins contain only one signal dot, even though it is near several other points (see **Figure 9**). These are most likely stationary clutter signals, but they are indistinguishable (based on histogram binning) from the moving target dots, which are well dispersed (low local density) in the magnitude–phase plane. To accurately measure the local density of these edge points, one must compute the number of dots within a magnitude–phase "distance" from the signal dot of interest. This procedure needs to be repeated for all signal dots (typically over several million), however, a highly computationally intensive task and unrealistic effort. Therefore, we propose a fine-tuning technique that uses the histogram-binning technique to first identify the moving target signal points and the edge clutter points and then apply the local density calculation only to these signal dots ("selective" calculations) to differentiate the well-dispersed moving target points from those of the clutter "edge". This dramatically reduces the number of calculations required and, most importantly, minimizes the number of "edge-points" false alarms without significantly degrading the performance of the detector or P_D. This procedure was applied to the same SAR ATI data used in **Figure 5**, and the output of the modified detector is shown in **Figure 10**. As can be seen, 18 out of 20 targets are detected, with a false alarm rate reduced to $P_{FA} = 2.53 \times 10^{-5}$, and the actual number of false alarms decreased from 10 to 4 (a 60% reduction). A slight degradation in the number of detected targets (from 19 to 18) is also noticed. This overall improvement may be desirable if one places a greater emphasis on reducing the number of false alarms over maximizing the number of detected targets.

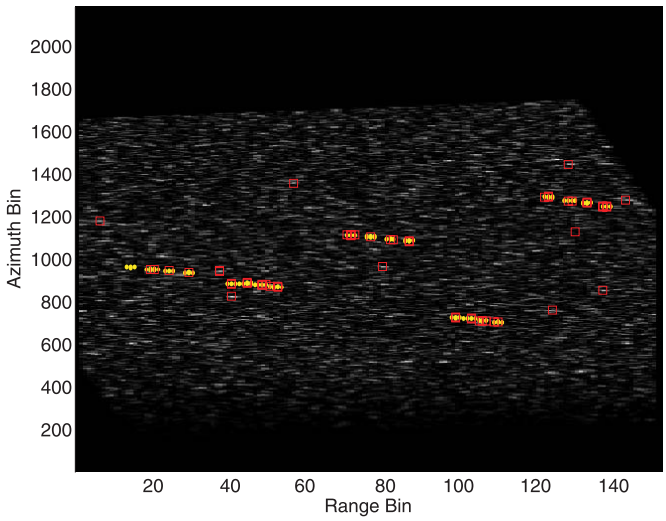

Figure 7. SAR ATI CFAR detector output, showing confirmed detected targets (yellow dot in open red square), missed targets (yellow dot), and false alarms (open red square).

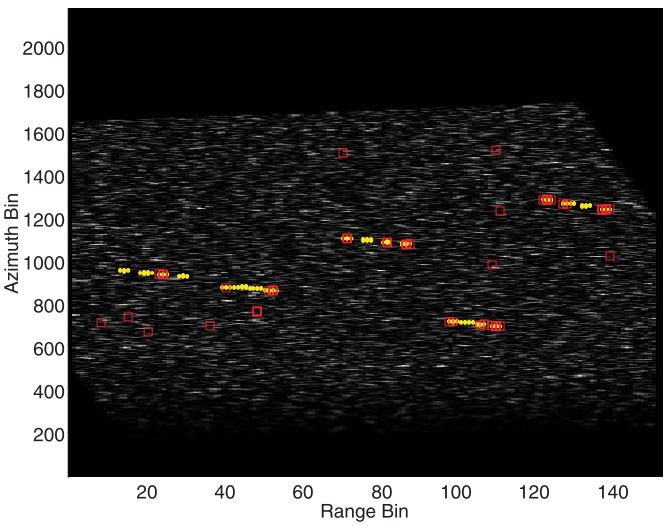

Figure 8. SAR ATI CFAR detection output via Gierull's marginal PDF method, showing confirmed detected targets (yellow dot in open red square), missed targets (yellow dot), and false alarms (open red square).

Airborne

Both original and modified CFAR detection schemes were also applied to the airborne data. The bell-shaped magnitude–phase distribution was obtained from the SAR ATI data and is plotted in **Figure 11**. There are five controlled moving targets and probably a few movers of opportunity in the imaged scene. Signal "dots" outside the main bell-shaped distribution most likely belong to these moving targets. To extract the movers, one applies the same histogram-binning procedure to this distribution and obtains density contour lines (see **Figure 12**) similar to those of the simulated data. All signal dots in magnitude–phase bins with a dot count equal to 1 (the

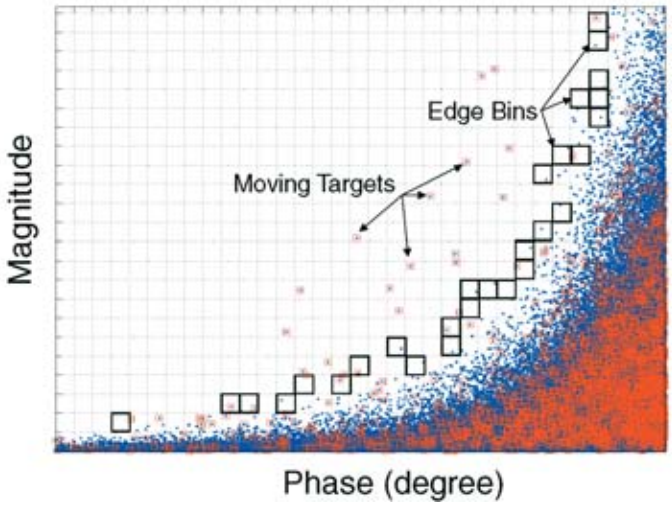

Figure 9. The tail of a magnitude–phase PDF, showing the edge points of the bell-shaped clutter distribution are indistinguishable from the more scattered moving target points (blue dot in open red square).

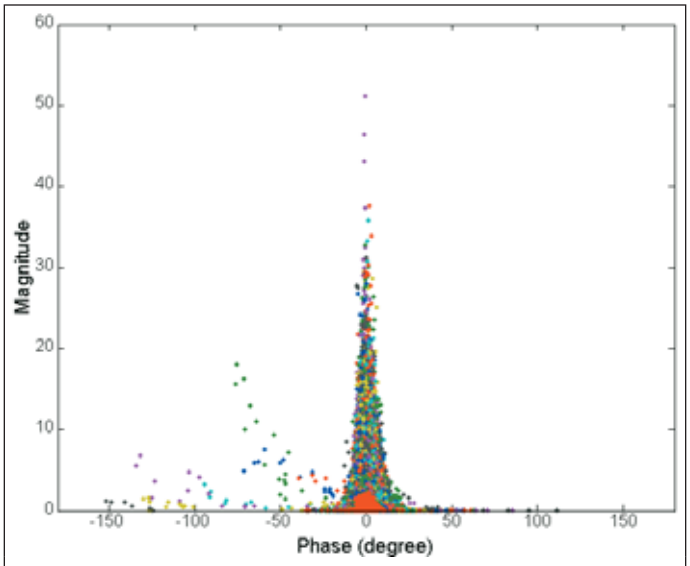

Figure 11. Magnitude versus phase of the airborne SAR ATI signal.

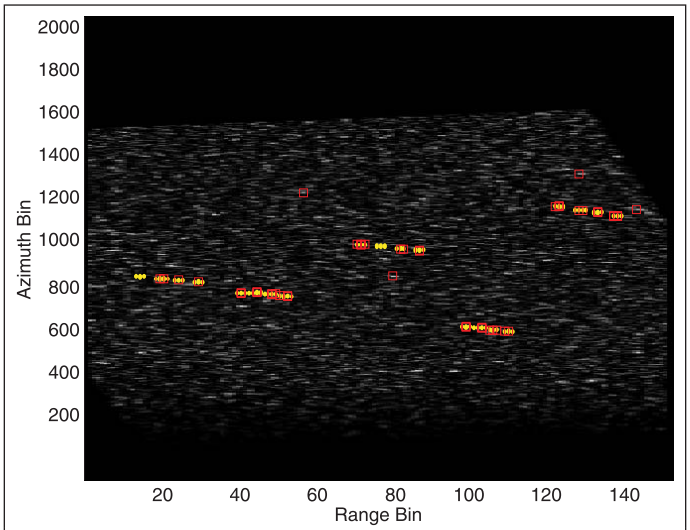

Figure 10. Modified SAR ATI detector output, showing confirmed detected targets (yellow dot in open red square), missed targets (yellow dot), and false alarms (open red square).

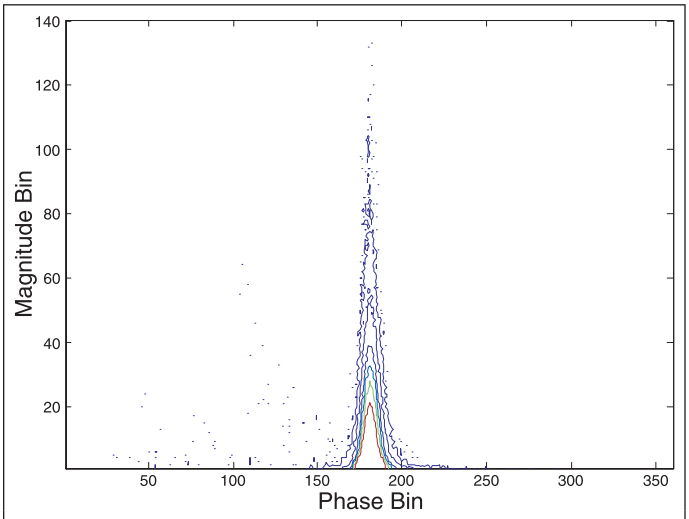

Figure 12. Two-dimensional histogram contour plot of magnitude–phase distribution of the airborne SAR ATI signal.

threshold) are considered to be mover signals (plus false alarms). The resulting GMTI image is shown in **Figure 13**. Dots with an arrow indicate confirmed detections of the controlled moving targets, those with a vertical line represent possible detections of targets of opportunity, and those alone are false alarms. Red dots indicate targets moving toward the radar, and green dots indicate targets moving away from the radar. Owing to velocity mismatch, the matched filter shifts the movers azimuthally. The arrows and vertical lines show the true positions of targets on a road or track. Four of the five controlled targets have been detected in all four imaging passes (P7–P10, where P7 is used for illustration), except for one case (P9) in which the detector missed the 70 km/h pickup truck on Steward Road. This is because of the mismatch between the terrain-matched filter and the target speed, which happens to fall on the first non-zero speed matched filter null, and as a consequence the target signal is severely attenuated by the filtering process. The detector also missed the MIT target because of the small RCS and low radial velocity of the target. The detector, however, detected two possible targets of opportunity on Highway 17. The overall performance of the detector is very good, even when it is applied to heterogeneous terrain. The modified detector, applied to the same SAR ATI data, shows similar performance improvement in reducing the number of false alarms (from 10 down to 6) while detecting the same number of moving targets (six movers detected; see **Figure 14**). The detections on the left-hand side of Highway 17 are most likely false alarms, since their ATI phase signs do not agree with the direction of their azimuth shifts. In addition,

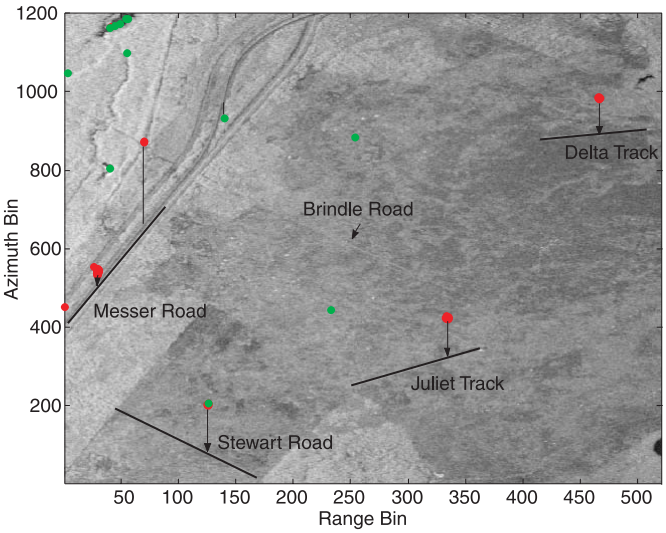

Figure 13. SAR ATI CFAR detector output: dot with an arrow denotes confirmed detection of the controlled targets; dot with an arrow and a vertical line denotes possible detection of targets of opportunity; and dot only denotes a false alarm. Red dots indicate targets moving toward the radar, and green dots targets moving away from the radar.

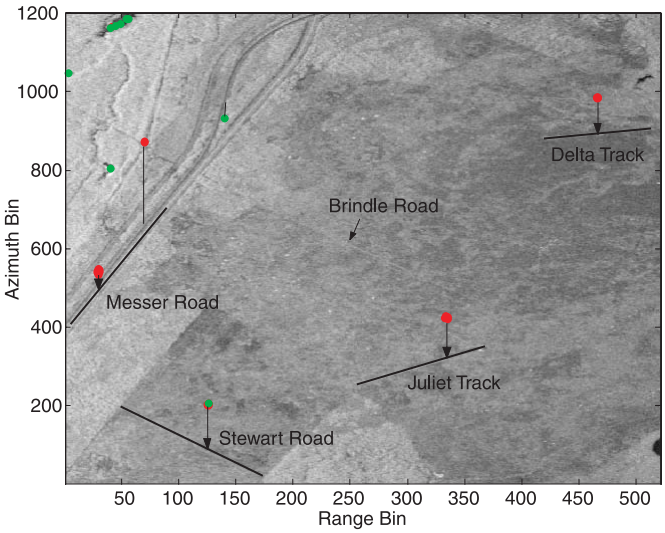

Figure 14. Modified SAR ATI CFAR detector output: dot with an arrow denotes confirmed detection of the controlled targets; dot with an arrow and a vertical line denotes possible detection of targets of opportunity; and dot only denotes a false alarm. Red dots indicate targets moving toward the radar, and green dots targets moving away from the radar.

their phase angles are small (less than 7°) but with large magnitudes. Therefore, these are bright but most likely stationary targets. Their small but nonzero phases are due to system phase noises. The proposed histogram-based detectors rely on the density of signal dots to differentiate between the stationary clutter and the moving targets. Since bright stationary targets appear as "rare events" in the imaged scene, they show up as dispersed signal dots (in the magnitude-phase plane), which protrude from the main bell-shaped distribution (see **Figures 11** and **12**) and are erroneously counted as moving targets by the detector, as indicated in a previous section. This is a shortcoming with this type of detection scheme, but it can be easily remedied with an additional phase notch filter, which disallows targets with phase values smaller than a certain phase threshold (estimated based on the system phase noise) to be counted as real movers, as discussed previously for Equation (12). Applying such a filter ($|\psi| > 7°$) to the output of the detector, the false alarms on the left side of the highway are eliminated. Dots clustered around a pond of water situated on the top left side of the imaged area are also false alarms, but these are likely due to the motion of the water. This phase shift is commonly observed in a SAR ATI image of a lake or river, and a simple phase filter cannot filter them out because the phase shift varies with the wind condition of the imaged area and reflects true motions in the scene. However, the image context should allow one to recognize them as false alarms.

Conclusion

One GMTI technique, currently being explored, is based on SAR along-track interferometry, which uses the magnitude–phase information of the interferogram to extract movers from stationary clutter. It was shown in Gierull (2001) that the marginal PDF of the magnitude of the interferogram, derived under the assumption of homogeneous clutter, does not agree with reality. Motivated by this discrepancy and by the difficulty of deriving a theoretical joint PDF that matches various terrain types, a fully automatic adaptive detection scheme, based on histogram approximation to the clutter joint PDF, has been proposed. The new method permits the implementation of a CFAR detector without the need to derive a theoretical joint PDF for the clutter interferogram. A false alarm reduction technique, based on "selective" local density calculations, was also discussed and (experimentally) verified, showing a striking improvement in reducing the number of false alarms (up to 60% reduction) without significantly degrading the detector performance. The detector was shown to be robust in its ability to handle both simulated (RADARSAT-2) and real (airborne) data. Preliminary comparison with a conventional parametric CFAR detector, derived using theoretical marginal PDFs of the magnitude and phase of the interferogram, showed the performance superiority of the new detector.

Acknowledgement

Special thanks to Dr. Chuck Livingstone, the RADARSAT-2 GMTI project leader, whose knowledge, experience, and guidance have enriched me tremendously throughout the years.

References

Chiu, S. 2000a. *An analysis of RADARSAT-2 SAR-GMTI performance for standard beam mode*. Defence Research Establishment Ottawa (DREO), Technical Report TR 2000-088.

Chiu, S. 2000b. *Performance of RADARSAT-2 SAR-GMTI processor at high SAR resolutions*. Defence Research Establishment Ottawa (DREO), Technical Report TR 2000-093.

Chiu, S., and Livingstone, C. 2005. A comparison of displaced phase centre antenna and along-track interferometry techniques for RADARSAT-2 ground moving target indication. *Canadian Journal of Remote Sensing*, Vol. 31, No. 1, pp. 37–51.

Conte, E., Longo, M., and Lops, M. 1991. Modeling and simulation of non-Rayleigh radar clutter. *Radar and Signal Processing, IEE Proceedings F*, Vol. 138, No. 2, pp. 121–130.

Ender, J.H.G. 1999. Space–time processing for multi-channel synthetic aperture radar. *Electronics & Communication Engineering Journal*, Vol. 11, pp. 29–38.

Frery, A.C., Müller, H.-J., Yanasse, C.C.F., and Sant'Anna, S.J.S. 1997. A model for extremely heterogeneous clutter. *IEEE Transactions on Geoscience and Remote Sensing*, Vol. 35, No. 3, pp. 648–659.

Gierull, C.H. 2001. *Statistics of SAR interferograms with application to moving target detection*. Defence Research Establishment Ottawa (DREO), Technical Report TR 2001-045.

Gierull, C.H., and Sikaneta, I. 2002. Estimating the effective number of looks in interferometric SAR data. *IEEE Transactions on Geoscience and Remote Sensing*, Vol. 40, No. 8, pp. 1733–1742.

Goodman, J.W. 1963. Statistical analysis based on a certain multivariate complex Gaussian distribution (an introduction). *Annals of Mathematical Statistics*, Vol. 34, No. 152, pp. 152–180.

Joughin, I.R., and Winebrenner, D.P. 1994. Effective number of looks for a multi-look interferometric phase distribution. In *IGARSS'94, Proceedings of the International Geoscience and Remote Sensing Symposium*, Pasadena, Calif., 8–12 August 1994. IEEE, New York. pp. 2276–2278.

Lee, J.-S., Hoppel, K.W., Mango, S.A., and Miller, A.R. 1994a. Intensity and phase statistics of multi-look polarimetric and interferometric SAR imagery. *IEEE Transactions on Geoscience and Remote Sensing*, Vol. 32, No. 5, pp. 1017–1028.

Lee, J.-S., Miller, A.R., and Hoppel, K.W. 1994b. Statistics of phase difference and product magnitude of multi-look processed Gaussian signals. *Waves in Random Media*, Vol. 5, pp. 307–319.

Livingstone, C.E. 1998. The addition of MTI modes to commercial SAR satellites. In *Proceedings of the 10th CASI Conference on Astronautics*, 26–28 Oct. 1998, Ottawa, Ont. Canadian Aeronautics and Space Institute, Ottawa, Ont. pp. 267–275.

Livingstone, C.E., Sikenata, I., Gierull, C.H., Chiu, S., Beaudoin, A., Campbell, J., Beaudoin, J., Gong, S., and Knight, T.A. 2002. An airborne synthetic aperture radar (SAR) experiment to support RADARSAT-2 ground moving target indication (GMTI). *Canadian Journal of Remote Sensing*, Vol. 28, No. 6, pp. 794–813.

Luscombe, A. 1995. The Radarsat Project. *IEEE Canadian Review*, Fall 1995, No. 21.

Marola, G. 1989. On the detection of the axes of symmetry of symmetric and almost symmetric planar objects. *IEEE Transactions on Pattern Analysis and Machine Intelligence*, Vol. 11, No. 1, pp. 104–108.

Moccia, A., and Rufino, G. 2001. Spaceborne along-track SAR interferometry: performance analysis and mission scenarios. *IEEE Transactions on Aerospace and Electronic Systems*, Vol. 37, No. 1, pp. 199–213.

Nohara, T.J., Premji, A., and Weber, P. 1999. *Final report: simulator — space based radar, Vol. I: requirements, design and user guide*. Defence Research Establishment Ottawa (DREO), Contractor Report DND/SST File No. W7714-8-0141.

Soumekh, M. 1997. Moving target detection in foliage using along-track monopulse synthetic aperture radar imaging. *IEEE Transactions on Image Processing*, Vol. 6, No. 8, pp. 1148–1163.